



The Value of Progenitor Radius Measurements for Explosion Modeling of Type II-Plateau Supernovae

Jared A. Goldberg¹ and Lars Bildsten^{1,2}

¹ Department of Physics, University of California, Santa Barbara, CA 93106, USA; goldberg@physics.ucsb.edu

² Kavli Institute for Theoretical Physics, University of California, Santa Barbara, CA 93106, USA

Received 2020 February 17; revised 2020 May 8; accepted 2020 May 14; published 2020 June 2

Abstract

Using Modules for Experiments in Stellar Astrophysics (MESA)+STELLA, we show that very different physical models can adequately reproduce a specific observed Type II-Plateau supernova (SN). We consider SN2004A, SN2004et, SN2009ib, SN2017eaw, and SN2017gmr, nickel-rich ($M_{\text{Ni}} > 0.03M_{\odot}$) events with bolometric lightcurves and a well-sampled decline from the plateau. These events also have constraints on the progenitor radius, via a progenitor image, or, in the case of SN2017gmr, a radius from fitting shock-cooling models. In general, many explosions spanning the parameter space of progenitors can yield excellent lightcurve and Fe-line velocity agreement, demonstrating the success of scaling laws in motivating models that match plateau properties for a given radius and highlighting the degeneracy between plateau luminosity and velocity in models and observed events, which can span over 50% in ejecta mass, radius, and explosion energy. This can help explain disagreements in explosion properties reported for the same event using different model calculations. Our calculations yield explosion properties when combined with pre-explosion progenitor radius measurements or a robust understanding of the outermost $<0.1M_{\odot}$ of material that quantifies the progenitor radius from SN observations a few days after explosion.

Unified Astronomy Thesaurus concepts: Massive stars (732); Type II supernovae (1731); Red supergiant stars (1775); Supernovae (1668); Hydrodynamical simulations (767); Radiative transfer simulations (1967); Stellar evolutionary models (2046); Light curves (918)

1. Introduction

Massive stars ($M \gtrsim 10M_{\odot}$) at the end of their evolution become red supergiants (RSGs) with radii of $\approx 400\text{--}1000R_{\odot}$, before ending their lives as core-collapse Type II-Plateau supernovae (Type IIP SNe) with lightcurves that plateau over ≈ 100 days. The progenitor radius (R), ejected mass (M_{ej}), explosion energy (E_{exp}), and ^{56}Ni mass (M_{Ni}) determine these lightcurves (e.g., Popov 1993; Sukhbold et al. 2016), and inferring these properties from observations could lend insight into which stars explode as SNe. Although early work provided scaling relations attempting to uniquely relate plateau properties and expansion velocities to explosion characteristics (e.g., Litvinova & Nadyozhin 1983; Popov 1993), recent work highlights the nonuniqueness of lightcurve and velocity modeling for a given SN after ≈ 20 days (Dessart & Hillier 2019; Goldberg et al. 2019; Martinez & Bersten 2019).

Building on Goldberg et al. (2019, hereafter GBP19), we verify these degeneracies by comparing explosions of very different progenitor models to nickel-rich ($M_{\text{Ni}} > 0.03M_{\odot}$) events with bolometric lightcurves, a well-sampled decline from the plateau, and constraints on the progenitor radius. We utilize the open-source 1D stellar evolution code Modules for Experiments in Stellar Astrophysics (MESA; Paxton et al. 2011, 2013, 2015, 2018, 2019) for our evolutionary and explosion models and the multigroup radiation-hydrodynamics instrument STELLA (Blinnikov et al. 1998, 2000, 2006) to produce lightcurves and model expansion velocities. Emission in the first 20 days depends on the radial density structure of the outer $<0.1M_{\odot}$ of matter around a vigorously convecting RSG progenitor (e.g., Morozova et al. 2016). SN emission during this time can be modified by the uncertain circumstellar environment (e.g., Morozova et al. 2017), and may reflect the

intrinsically 3D structure of these outer layers (see, e.g., Chiavassa et al. 2011). Therefore, we restrict our analysis to observations after day ≈ 20 , when emission comes from the bulk of the stellar envelope. However, we still show our results for earlier times, where the qualitative trends may hold.

2. Observed SNe and Their Degeneracy Curves

GBP19 showed that Type IIP SNe with ^{56}Ni mass ($M_{\text{Ni}} \geq 0.03M_{\odot}$), luminosity at day 50 (L_{50}), and plateau duration (t_p) can approximately yield the ejected mass ($M_{10} \equiv M_{\text{ej}}/10M_{\odot}$) and asymptotic explosion energy ($E_{51} \equiv E_{\text{exp}}/10^{51}\text{ erg}$) as a function of progenitor radius ($R_{500} \equiv R/500R_{\odot}$), via the following relations:

$$\begin{aligned} \log(E_{51}) &= -0.728 + 2.148 \log(L_{42}) - 0.280 \log(M_{\text{Ni}}) \\ &\quad + 2.091 \log(t_{p,2}) - 1.632 \log(R_{500}), \\ \log(M_{10}) &= -0.947 + 1.474 \log(L_{42}) - 0.518 \log(M_{\text{Ni}}) \\ &\quad + 3.867 \log(t_{p,2}) - 1.120 \log(R_{500}), \end{aligned} \quad (1)$$

where M_{Ni} is in units of M_{\odot} , $L_{42} = L_{50}/10^{42}\text{ erg s}^{-1}$ and $t_{p,2} = t_p/100$ days, and \log is base 10. Moreover, because expansion velocities inferred from the Fe II 5169 Å line are determined by line-forming regions near the photosphere, velocity data during the plateau period do not break this degeneracy ($L_{50} \propto v_{50}^2$; Hamuy & Pinto 2002; Kasen & Woosley 2009). Rather, SNe with the same L_{50} , t_p , and M_{Ni} and similar expansion velocities during the plateau can be realized by a family of explosions with a range of R , E_{exp} , and M_{ej} obeying the Equation (1) relations.

2.1. Measuring Nickel Mass and Plateau Duration of Type IIP SNe

We estimate the plateau duration t_p following Valenti et al. (2016), fitting the functional form $y(t)$ to the bolometric luminosity (L_{bol}) around the fall from the plateau:

$$y(t) \equiv \log(L_{\text{bol}}) = \frac{-A_0}{1 + e^{(t-t_p)/w_0}} + (P_0 \times t) + M_0. \quad (2)$$

We use the python routine `scipy.optimize.curve_fit` to fit the lightcurve starting when the luminosity evolution is 75% of the way to its steepest descent, fixing P_0 to be the slope on the ^{56}Ni tail (GBP19). The fitting parameter t_p is the plateau duration. We also extract the ^{56}Ni mass from L_{bol} by calculating the cumulative observable ET (Nakar et al. 2016), which corresponds to the total time-weighted energy radiated away in the SN generated by the initial shock and not by ^{56}Ni decay:

$$ET_c(t) = \int_0^t t' [L_{\text{bol}}(t') - Q_{\text{Ni}}(t')] dt', \quad (3)$$

where t is the time in days since the explosion and

$$Q_{\text{Ni}} = \frac{M_{\text{Ni}}}{M_{\odot}} (6.45e^{-t'/t_{\text{Ni}}} + 1.45e^{-t'/\tau_{\text{Co}}}) \times 10^{43} \text{ erg s}^{-1} \quad (4)$$

is the $^{56}\text{Ni} \rightarrow ^{56}\text{Co} \rightarrow ^{56}\text{Fe}$ decay luminosity given by Nadyozhin (1994), equivalent to the heating rate of the ejecta assuming complete trapping with $t_{\text{Ni}} = 8.8$ days and $\tau_{\text{Co}} = 111.3$ days. As $t \rightarrow \infty$ and all shock energy has radiated away, the slope of the ET_c curve on the ^{56}Co decay tail should be zero when the estimate of M_{Ni} is correct. This method yields excellent agreement between the resulting model lightcurve tails and observed lightcurves, and with the ^{56}Co decay luminosity (Nadyozhin 1994):

$$L(t \rightarrow \infty) = 1.45 \times 10^{43} \exp\left(-\frac{t}{\tau_{\text{Co}}}\right) \frac{M_{\text{Ni}}}{M_{\odot}} \text{ erg s}^{-1}. \quad (5)$$

2.2. SN Selection

In order to further explore this degeneracy, we apply these scalings to five observed SNe: SN2004A, SN2004et, SN2009ib, SN2017eaw, and SN2017gmr.

SN2004A was discovered by K. Itagaki on 2004 January 9 in NGC 6207 (Hendry et al. 2006). Following Pejcha & Prieto (2015) we adopt an explosion date of MJD 53001.53. Progenitor observations indicate $\log(L_p/L_{\odot}) = 4.9 \pm 0.3$ and $T_{\text{eff}} = 3890 \pm 375$ K, implying a radius of $\approx 625R_{\odot}$ (Smartt 2015). From the Pejcha & Prieto (2015) bolometric lightcurve, we get $\log(L_{42}) = -0.07$. Estimates for the ^{56}Ni mass include $M_{\text{Ni}}/M_{\odot} = 0.050^{+0.040}_{-0.020}$ from points on the bolometric-corrected V-band tail and $M_{\text{Ni}}/M_{\odot} = 0.042^{+0.017}_{-0.013}$ comparing to the tail of 1987A, which the original authors average to yield $M_{\text{Ni}}/M_{\odot} = 0.046^{+0.0031}_{-0.017}$ (Hendry et al. 2006). We measure a plateau duration of $t_p = 124$ days and use $M_{\text{Ni}} = 0.042M_{\odot}$.

SN2004et was discovered in NGC 6946 by S. Moretti on 2004 September 27, with a well-constrained explosion date of 2004 September 22.0 (MJD 53270.0; Li et al. 2005). There is some disagreement in the literature about the progenitor (see Smartt 2009 and Davies & Beasor 2018) since follow-up

imaging shows R- and I-band flux excesses in the location of the inferred progenitor in Hubble Space Telescope (HST) pre-imaging (Crockett et al. 2011). As a result, Martinez & Bersten (2019) report a progenitor radius of $350R_{\odot}$ – $980R_{\odot}$. We adopt the bolometric lightcurve given by Martinez & Bersten (2019), which indicates $\log(L_{42}) = 0.27$. Estimates for the ^{56}Ni mass include $M_{\text{Ni}}/M_{\odot} = 0.048 \pm 0.01$ from the scaled ^{56}Co decay tail of 1987A to $M_{\text{Ni}} = 0.06 \pm 0.02$ estimated using V-magnitudes from 250 to 315 days (Sahu et al. 2006). We measure $t_p = 123.1$ days and use $M_{\text{Ni}} = 0.063M_{\odot}$.

SN2009ib was discovered by the Chilean Automatic Supernova Search on 2009 August 6.30 in NGC 1559, with an estimated explosion date of MJD 55041.3 (Takáts et al. 2015). HST pre-images indicate either a yellow source with $\log(L_p/L_{\odot}) = 5.04 \pm 0.2$, or possibly a fainter RSG with $\log(L_p/L_{\odot}) = 5.12 \pm 0.14$ and $R \approx 1000R_{\odot}$ assuming $T_{\text{eff}} \approx 3400$ K (Takáts et al. 2015). This event is peculiar in that there is a shallow drop from the plateau luminosity to the ^{56}Co decay tail, falling noticeably off of the Müller et al. (2017) relation between L_{50} and M_{Ni} . From the Takáts et al. (2015) lightcurve, we measure $\log(L_{42}) = -0.33$ and $M_{\text{Ni}}/M_{\odot} = 0.043$, and $t_p = 139.8$, days. Nakar et al. (2016) also highlighted that this event had a ratio of the integrated ^{56}Ni decay chain energy to integrated shock energy of $\eta_{\text{Ni}} = 2.6$, much larger than typical values of $\eta_{\text{Ni}} \approx 0.2$ – 0.6 (e.g., η_{Ni} for SN1999em ≈ 0.54).

SN2017eaw was discovered by P. Wiggins on 2017 May 14.238 in NGC 6946, with an estimated explosion date of MJD 57886.0 (Szalai et al. 2019). Pre-explosion imaging suggests $\log(L_p/L_{\odot}) = 4.9 \pm 0.2$ and $T_{\text{eff}} = 3350^{+450}_{-250}$ K, corresponding to $R \approx 845R_{\odot}$, obscured by a $> 2 \times 10^{-5}M_{\odot}$ dust shell extending out to $4000R_{\odot}$ (Kilpatrick & Foley 2018), assuming the distance to NGC 6946 to be $D = 6.72 \pm 0.15$ Mpc (from the tip of the red giant branch (TRGB) by Tikhonov 2014).³ We adopt the bolometric lightcurve of Szalai et al. (2019) using $D = 6.85$ Mpc, although more recent TRGB measurements suggest $D = 7.72 \pm 0.78$ Mpc (van Dyk et al. 2019). Estimates for the ^{56}Ni mass assuming $D = 6.85$ Mpc range from $M_{\text{Ni}}/M_{\odot} = 0.036$ – 0.045 (Szalai et al. 2019) to $M_{\text{Ni}} = 0.05M_{\odot}$ (Tsvetkov et al. 2018). From the Szalai et al. (2019) lightcurve, we measure $t_p = 117.2$ days, $M_{\text{Ni}} = 0.048M_{\odot}$, and $\log(L_{42}) = 0.21$.

SN2017gmr occurred in NGC 988, discovered on MJD 58000.266 during the DLT40 SN search with the explosion epoch assumed to be MJD 57999.09 at $D = 19.6 \pm 1.4$ Mpc (Andrews et al. 2019). No progenitor detection was made, but shock-cooling modeling of the early SN recovers $R \approx 500R_{\odot}$. Andrews et al. (2019) find $M_{\text{Ni}} = 0.13 \pm 0.026M_{\odot}$ assuming all late-time luminosity comes from Ni decay, although multi-peaked emission lines emerging after day 150 suggest asymmetries are present either in the core's explosion or in late-time interaction with the surrounding environment. We adopt the Andrews et al. (2019) bolometric lightcurve, and measure $\log(L_{42}) = 0.57$, $M_{\text{Ni}}/M_{\odot} = 0.13$, and $t_p = 94.5$ days.

2.3. The Degeneracy Curves

The families of explosion parameters recovered by inserting each SN's M_{Ni} , L_{50} , and t_p into Equation (1) are shown in

³ See also Rui et al. (2019), who infer a radius of $636 \pm 155R_{\odot}$ from early SN temperature observations (consistent with the progenitor SED), in an expanding dusty environment.

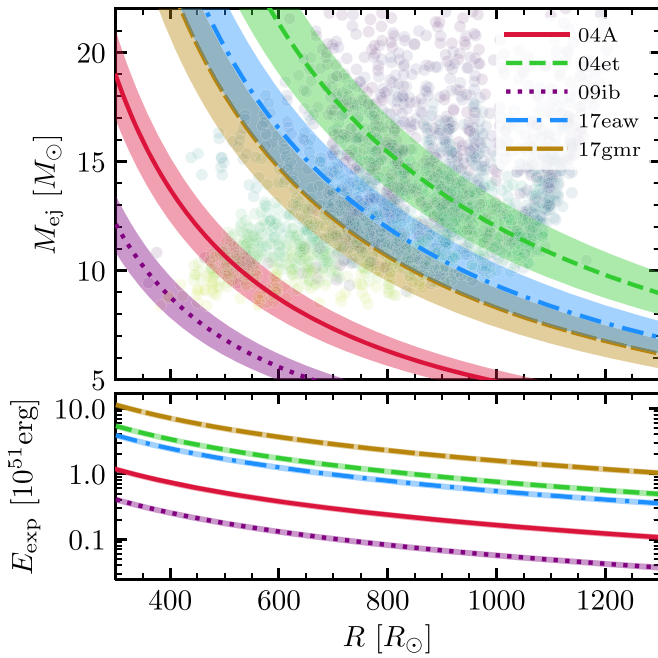


Figure 1. Degeneracy curves for M_{ej} (top) and E_{exp} (bottom) recovered from Equation (1) as a function of R for the observed SNe considered here. Shaded solid-color regions correspond to the $\approx 11\%$ rms deviations between the models of GBP19 and their recovered parameters. Additional observational uncertainties are not included. The M_{ej} and R of 2179 progenitor models are also shown in the background, with color ranging from yellow to purple tracking $M_{\text{ZAMS}} = 10\text{--}25M_{\odot}$.

Figure 1 as a function of R . Also shown is a large suite of RSG progenitor models to demonstrate the potential variety of M_{ej} and R within reasonable stellar evolution assumptions. For each event, M_{ej} and E_{exp} can be inferred from the plot for a given R .

The progenitor models were constructed using MESA revision 10398, and evolved to Fe core infall, following the `example_make_pre_ccsn` test case described in detail by Paxton et al. (2018, hereafter MESA IV). We varied the initial mass ($M_{\text{ZAMS}}/M_{\odot} = 10.0\text{--}15.0$ in increments of $0.5M_{\odot}$, and $15.0\text{--}25.0$ in increments of $1.0M_{\odot}$), surface rotation ($\omega/\omega_{\text{crit}} = 0.0; 0.2$), mixing length α in the H-rich envelope ($\alpha_{\text{env}} = 2.0; 3.0; 4.0$), core overshooting ($f_{\text{ov}} = 0.0; 0.01; 0.018$), and wind efficiency ($\eta_{\text{wind}} = 0.1\text{--}1.0$, increments of 0.1) using MESA’s “Dutch” wind scheme. All models had $Z = 0.02$. Only models that reached Fe core infall are shown. Rather than one relationship between M_{ej} and R , this set of models suggests a wide range in which RSGs can exist. This diversity reflects the importance of winds in determining the final masses and radii of stellar models (Renzo et al. 2017), and supports recent work showing diversity in progenitor masses for comparable positions on the H-R diagram (Farrell et al. 2020).

3. Explosion Models and Comparison to Observations

We then select progenitor models to explode in order to match observations guided by Equation (1) applied to an SN’s respective L_{42} , M_{Ni} , and t_p . For SNe 2004A, 2004et, SN2017eaw, and 2017gmr, we chose three progenitor models each, consistent with the respective degeneracy curves in Figure 1, with ejecta masses near the larger- M_{ej} , middle- M_{ej} , and smaller- M_{ej} intersections of the theoretical curves and the progenitor model suite. For SN2017eaw, we chose three

additional models consistent with a distance 10% farther away (i.e., increasing L_{50} and M_{Ni} by 21%, not shown in Figure 1). Very low M_{ej} and radii are recovered for SN2009ib, with little overlap with our progenitor grid, so we exploded only two progenitors, one off the grid ($\alpha = 6$). Properties of these models at the moment of explosion, input physics, and values for M_{Ni} are shown in Table 1. Also shown are the time to shock breakout (t_{sb}) and the mass above the photosphere at day 20 ($\delta m_{\text{ph},20}$).

We then excised the Fe cores with an entropy cut of $4 \text{ erg g}^{-1} \text{ K}^{-1}$, and exploded these models using MESA with Duffell RTI (Duffell 2016) and the fallback estimation technique described in Appendix A of GBP19, with an additional velocity cut of 500 km s^{-1} at handoff to STELLA at shock breakout.⁴ All explosions resulted in negligible fallback. At shock breakout, we rescaled the ^{56}Ni distribution to match the desired M_{Ni} , and imported the ejecta profile into STELLA to model the evolution post-shock-breakout. We used 400 spatial zones and 40 frequency bins in STELLA, which yields convergence in bolometric lightcurves on the plateau (see Figure 30 of MESA IV and the surrounding discussion). For SN2017eaw at 6.85 Mpc, we used 800 spatial zones in order to more faithfully capture the outermost layers of the ejecta. Because we are focused on matching plateau emission from the bulk of the ejecta, occurring after day ≈ 20 , we do not include any extra material beyond the progenitor photosphere for most of our model lightcurves.

3.1. Comparison to Observed SNe

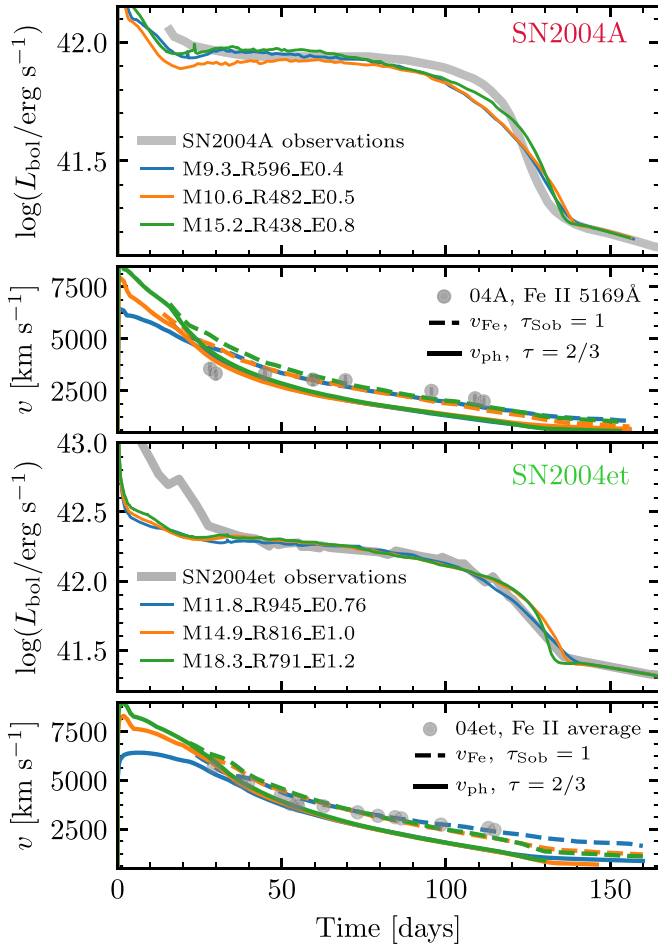
Despite intrinsic scatter amounting to $\approx 11\%$ rms deviations between model parameters and M_{ej} and E_{exp} recovered from Equation (1) applied to model radii and lightcurves (GBP19), computations approximately obeying Equation (1) produce bolometric lightcurves that match the observations. Figure 2 shows the results for SN2004A (top two panels) and SN2004et (bottom two panels). Both SN2004A and SN2004et exhibit good agreement between models, lightcurves, and velocity evolution on the plateau, with no model being the “best fit” for either event. Photospheric velocities at very early times ($\lesssim 20$ days) do differ between different models, with more compact, higher- E_{exp} models yielding faster early-time velocities. However, velocity measurements before day 20 are rare, and at these times velocities might be modified by the circumstellar environment (e.g., Moriya et al. 2018). The early observed lightcurve ($\lesssim 30$ days) of SN2004et also exhibits a clear luminosity excess compared to the lightcurve models. Such excess is often attributed to interaction with an extended envelope or wind, or with pre-SN outbursts (e.g., Morozova et al. 2017, 2020).

All three models for SN2004et are consistent with the reported $R = 350\text{--}980R_{\odot}$. For SN2004A, only the low-mass/low-energy model M9.3_R596_E0.4 is consistent with the progenitor observations, and we conclude for that SN that $M_{\text{ej}} \lesssim 10M_{\odot}$ and $E_{\text{exp}} \lesssim 0.4 \times 10^{51} \text{ erg}$.

⁴ For all models except 2017eaw at 6.85 Mpc, MESA revision 10925 was used, as in GBP19. Because we consider excess emission in the early lightcurve of 2017eaw at 6.85 Mpc, revision 11701 was used with a dense mesh near the surface set by “`split_merge_amr_logtau_zoning=.true.`” in `inlist_controls` to ensure that the outer region is adequately resolved.

Table 1
Model Properties

SN Name (M_{Ni}/M_{\odot})	Model Name ($M_{\text{ej},\odot}$) (R_{\odot}) (E_{51})	M_{ZAMS} (M_{\odot})	$f_{\text{ov}}, \alpha_{\text{env}}, \omega/\omega_{\text{crit}}, \eta_{\text{w}}$	M_{final} (M_{\odot})	$M_{\text{c,f}}$ (M_{\odot})	$M_{\text{c,He}}$ (M_{\odot})	$\log\left(\frac{L_{\text{p}}}{L_{\odot}}\right)$	T_{eff} (K)	t_{sb} (days)	$\delta m_{\text{ph},20}$ (M_{\odot})
2004A (0.042)	M9.3_R596_E0.4	11.5	0.018, 3.0, 0.0, 0.5	10.87	1.62	3.79	4.86	3900	1.6	0.032
	M10.6_R482_E0.5	12.5	0.01, 4.0, 0.0, 0.2	12.28	1.64	3.89	5.20	5250	1.2	0.061
	M15.2_R438_E0.8	17.0	0.0, 4.0, 0.0, 0.2	16.66	1.48	5.33	5.23	5610	1.0	0.096
2004et (0.063)	M11.8_R945_E0.76	14.0	0.018, 2.0, 0.2, 0.2	13.42	1.59	4.89	5.22	3790	2.2	0.031
	M14.9_R816_E1.0	18.0	0.0, 2.0, 0.0, 0.5	16.53	1.62	5.85	5.44	4640	1.8	0.036
	M18.3_R791_E1.2	22.0	0.0, 3.0, 0.0, 0.5	19.89	1.55	7.70	5.25	4160	1.7	0.040
2009ib (0.043)	M7.86_R375_E0.23	10.0	0.018, 4.0, 0.2, 0.7	9.41	1.55	3.15	5.05	5450	1.1	0.074
	M10.2_R356_E0.3	12.0	0.01, 6.0, 0.2, 0.4	11.65	1.48	3.69	3.99	3040	1.1	0.082
2017eaw at 6.85Mpc (0.048)	M10.2_R850_E0.65	13.5	0.01, 2.0, 0.2, 0.8	11.99	1.77	4.24	4.92	3370	2.0	0.032
	M12.7_R719_E0.84	15.0	0.01, 3.0, 0.0, 0.2	14.53	1.80	5.09	5.04	3910	1.7	0.036
	M17.2_R584_E1.3	20.0	0.0, 4.0, 0.0, 0.4	18.92	1.70	6.79	5.10	4490	1.2	0.072
2017eaw, mod. at 7.54Mpc (0.0581)	M11.9_R849_E0.9	14.0	0.016, 2.0, 0.0, 0.2	13.64	1.70	4.55	5.08	3690	1.8	0.032
	M15.7_R800_E1.1	19.0	0.0, 3.0, 0.2, 0.4	17.33	1.66	6.83	5.18	4040	1.7	0.041
	M19.0_R636_E1.5	22.0	0.0, 4.0, 0.0, 0.2	20.51	1.55	7.74	5.54	5550	1.2	0.056
2017gmr (0.13)	M9.5_R907_E1.9	12.0	0.018, 2.0, 0.2, 0.6	11.01	1.48	3.86	5.70	5110	1.1	0.076
	M12.5_R683_E3.0	14.5	0.01, 3.0, 0.0, 0.2	14.09	1.55	4.80	5.46	5120	0.81	0.11
	M16.5_R533_E4.6	19.0	0.0, 4.0, 0.0, 0.4	18.09	1.57	6.28	5.29	5250	0.55	0.22

**Figure 2.** Lightcurves and Fe-line velocities for SN2004A (top two panels) and SN2004et (bottom two panels). Gray markers correspond to the observations, and colored lines correspond to explosion models, ordered in ascending M_{ej} and E_{exp} , and descending R .

3.2. SN2017eaw at Two Distances

To show the impact of changing the assumed distance on our modeling, we model SN2017eaw at two different distances: 6.85 Mpc, using the fiducial Szalai et al. (2019) lightcurve, and at 7.54 Mpc, with the same t_{p} but with 21% brighter L_{bol} and $M_{\text{Ni}} = 0.0581 M_{\odot}$. Models were selected to match Equation (1) with the appropriate L_{42} , t_{p} , and M_{Ni} for each distance. Figure 3 compares models to observations. The top two panels correspond to $D = 6.85$ Mpc, and the bottom two panels to $D = 7.54$ Mpc.⁵ Like SN2004A and SN2004et, models agree well with the data, and agreement in L_{50} also yields agreement in the velocity of the models after day ≈ 20 . Agreement between models and *both* velocity and luminosity data is better for $D = 7.54$ Mpc. For $D = 6.85$ Mpc, two of our models, M10.2_R850_E0.65 and M12.7_R719_E0.84, match the progenitor properties within the uncertainties. At a 10% farther distance, assuming 21% brighter L_{p} and the same T_{eff} , only our M11.9_R849_E0.9 model is consistent with the updated progenitor properties. Assuming the measured progenitor radius of $845 R_{\odot}$, we chose models with $R \approx 850 R_{\odot}$ for both distances. The 10% greater distance leads to $\approx 17\%$ increase in M_{ej} , from $10.2 M_{\odot}$ to $11.9 M_{\odot}$ and $\approx 40\%$ increase in E_{exp} , from 0.65×10^{51} erg to 0.9×10^{51} erg.

For $D = 6.85$ Mpc, we also show lightcurves with and without a dense wind to reproduce the early excess emission (top two panels of Figure 3). We affix a wind density profile with total mass M_{wind} and $\rho_{\text{wind}}(r) = \dot{M}_{\text{wind}}/4\pi r^2 v_{\text{wind}}$, where \dot{M}_{wind} is a constant, and v_{wind} is the wind velocity. We varied $\dot{M}_{\text{wind}} = (0.1, 0.2, 0.3, 0.4) M_{\odot} \text{ yr}^{-1}$ and $v_{\text{wind}} = (3, 5, 8, 12) \text{ km s}^{-1}$ with M_{wind} from 0.2 to $0.8 M_{\odot}$.

⁵ The farther distance was motivated by the fact that velocities of models matching L_{50} and t_{p} of the fiducial distance are $\approx 10\%$ discrepant with observed velocities. Since $L_{50} \propto D^2 \propto v_{\text{Fe},50}^2$ (Hamuy & Pinto 2002; Kasen & Woosley 2009; GBP19), an intrinsically brighter SN at a distance $\approx 10\%$ further produces models that better match the velocity data. This distance is also consistent with a recent TRGB estimate of 7.72 ± 0.78 Mpc (van Dyk et al. 2019).

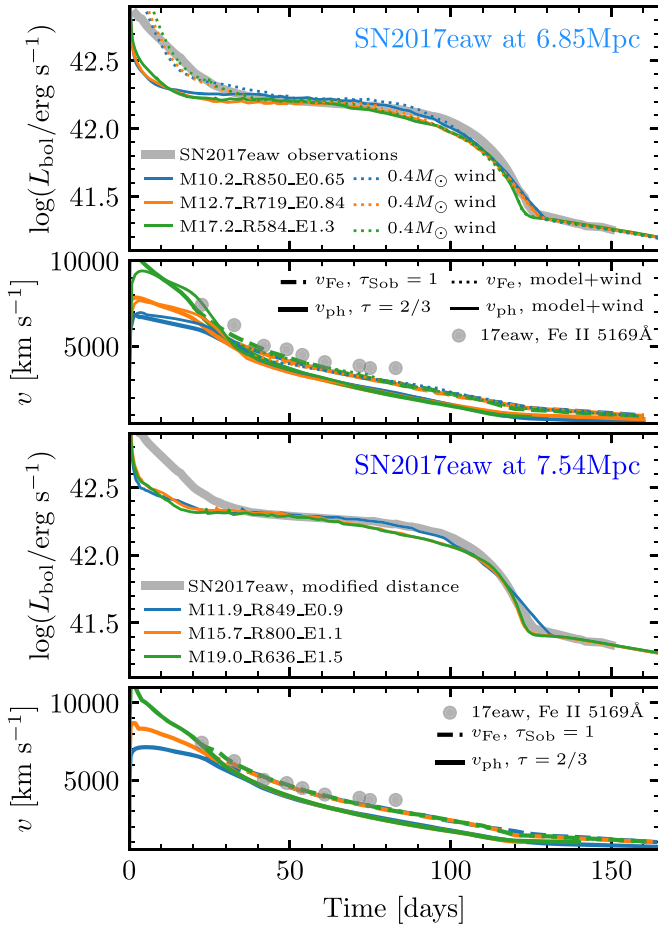


Figure 3. Lightcurves and Fe-line velocities for observations and models of SN2017eaw at $D = 6.85$ Mpc (top two panels) and $D = 7.54$ Mpc (bottom two panels). Gray markers correspond to observations, and colored lines correspond to explosion models. Colored dotted lines in the upper panels correspond to models with an additional $0.4M_{\odot}$ wind ($v_{\text{wind}} = 8 \text{ km s}^{-1}$, $\dot{M}_{\text{wind}} = 0.2 M_{\odot} \text{ yr}^{-1}$).

In the top of Figure 3 we show values of $v_{\text{wind}} = 8 \text{ km s}^{-1}$, $\dot{M}_{\text{wind}} = 0.2 M_{\odot} \text{ yr}^{-1}$, and $M_{\text{wind}} = 0.4 M_{\odot}$. We find that the same wind parameters produce comparable early excesses when added to the three degenerate lightcurves, suggesting that the excess is set by properties of the wind itself and the underlying lightcurve, rather than, e.g., E_{exp} . This wind also modifies the early velocity evolution. We do not claim that this is the only way to reproduce the early excess, as a variety of other outer density profiles can give rise to similar early excesses without affecting plateau properties (e.g., Morozova et al. 2020).

3.3. Modeling Challenges

For two events, SN2009IB and SN2017gmr, we see general agreement between models and bulk properties of the lightcurves (L_{50} and t_p), with distinct differences shown in Figure 4. Specifically, these models differ beyond an early luminosity excess that might be explained by pulsations, a wind, varied structure of the extended stellar atmosphere, or other early interaction.

In SN2009ib (top two panels of Figure 4), the relatively low luminosity and high ^{56}Ni heating yield lightcurve models that rise significantly between days 20 and 80. The narrow overlap between Equation (1) and our model grid suggests low M_{ej} and

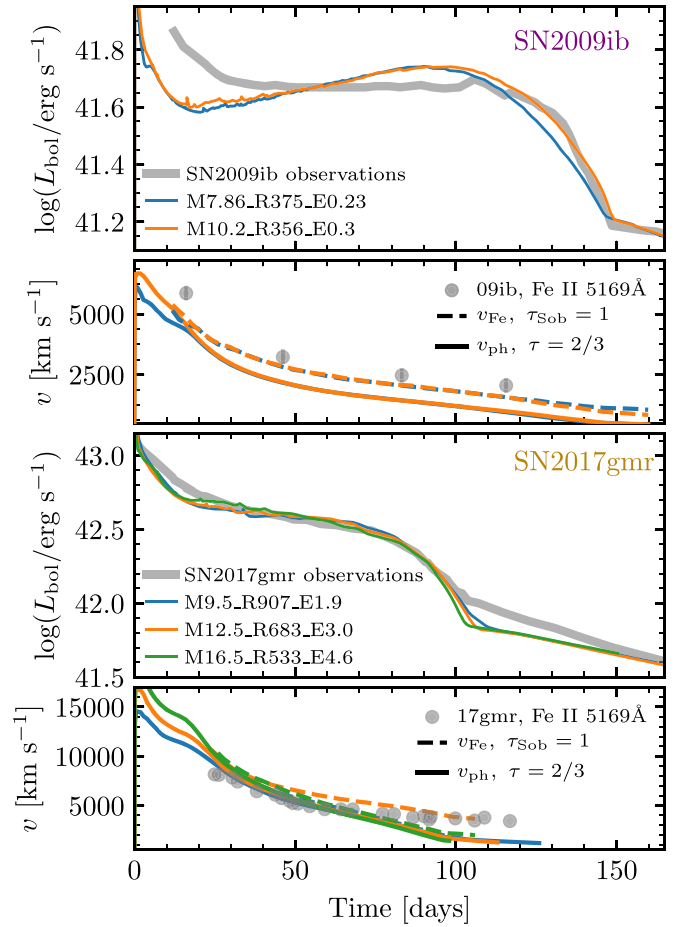


Figure 4. Lightcurves and Fe-line velocities for SN2009ib (top two panels) and SN2017gmr (bottom two panels). Gray markers correspond to observations, and colored lines correspond to explosion models.

small R . For a reasonable range of R , explosion energies recovered are also low ($E_{51} \approx 0.2\text{--}0.3$). The disagreement between the models and the velocity data may indicate that L_{bol} is underestimated in some way (see the discussion in Section 3.2). However, we found that additional models consistent with the velocity data and a brighter lightcurve of the same t_p still exhibit a similar, slightly shallower positive plateau slope. It is also possible that the estimated explosion epoch is too early. Moreover, neither explosion is consistent with an RSG of $R \approx 1000 R_{\odot}$ (derived assuming $T_{\text{eff}} = 3400 \text{ K}$), as $R = 1000 R_{\odot}$ implies exceedingly low $M_{\text{ej}} \approx 3 M_{\odot}$ and $E_{\text{exp}} \approx 6 \times 10^{49} \text{ erg}$. However, model M7.86_R375_E0.23 is able to reproduce the observed $\log(L_p/L_{\odot}) = 5.04 \pm 0.2$ with $T_{\text{eff}} \approx 5450 \text{ K}$, thus favoring the yellower source scenario.

For SN2017gmr (bottom two panels of Figure 4), all models agree equally well with the lightcurve, but indicate an excess in observed luminosity after the plateau as the lightcurve transitions to the ^{56}Co -decay tail. Observed velocities are taken from the reported Fe-line radius evolution, and are only shown before day 120, after which point the evolution is not photospheric. The slight disagreement between modeled and observed velocities suggests that perhaps the distance is overestimated, but modeling to match a fainter bolometric lightcurve provides no change in the apparent late-time excess.

Although this event has no progenitor pre-image, if R at the time of explosion is consistent with $\approx 500 R_{\odot}$ recovered from

fitting shock-cooling models to the photometric bands (Andrews et al. 2019), Equation (1) implies an enormous $E_{\text{exp}} \approx 5 \times 10^{51}$ erg! Our 533 R_{\odot} progenitor model indeed matches L_{50} and t_p when exploded with 4.6×10^{51} erg, shown in green in the lower two panels of Figure 4.

Our modeling procedure only considers matching L_{50} and t_p . To compare directly to the day 1 results in Andrews et al. (2019, Figure 9), we re-ran the SN2017gmr models with a surface resolution adequate to resolve emission at day 1 ($\delta m_{\text{ph}} \sim 10^{-3}$ – $10^{-4} M_{\odot}$). All three of our models yield luminosities at 1 day post-shock-breakout (L_1) a factor of ≈ 2 lower than L_1 of SN2017gmr recovered by their Sapir & Waxman (2017) shock-cooling model fits. Of our models, the day 1 photospheric temperature (T_1) of M16.5_R533_E4.6 does come closest to the reported shock-cooling $T_1 = 25,900$ K, with $T_1 \approx 27,000$ K, as compared to 29,000 K for M12.5_R683_E3.0 and 30,000 K for M9.5_R907_E1.9. At this time in the lightcurve evolution, the emitting region is coincident with the location of a density inversion in the stellar models, which is the focus of current ongoing studies.

For the lightcurve morphological differences, we have no easily available remedy without additional free parameters. Because we use the Duffell (2016) mixing prescription with coefficients calibrated to the 3D simulations as recommended in MESA IV, the resulting smoothing of the density profile and compositional mixing are held “fixed.” Nonetheless, the Equation (1)-motivated models agree well with the L_{50} and t_p observations.

4. Conclusions

The capability of MESA+STELLA to model observed SNe was introduced in MESA IV and demonstrated there and by Ricks & Dwarkadas (2019) to model a few Type IIP SNe. GBP19 introduced scaling relation (Equation (1)) fit from a suite of MESA+STELLA models in order to guide explosion modeling efforts for an observed SN lightcurve with a given L_{50} , t_p , and M_{Ni} . In the absence of understanding in models of the first 20 days, our application of these relations to the observed SNe 2004A, 2004et, 2009ib, 2017eaw, and 2017gmr shows families of explosion models that match the data for a wide range of M_{ej} , R , and E_{exp} . These degeneracies will not be easily lifted without an observed progenitor radius (and understanding the progenitor’s variability; see Goldberg et al. 2020) or other constraints. However, when combined with a radius given by progenitor pre-imaging or fitting the shock-cooling phase, we show that explosion models can be constrained following $E_{\text{exp}} \propto R^{-1.63}$ and $M_{\text{ej}} \propto R^{-1.12}$.

If there was confidence in stellar evolutionary input constraining an R – M_{ej} relation at the time of explosion, then these degeneracies could be broken, as assumed in the population synthesis/lightcurve modeling of Eldridge et al. (2019). However, when varying rotation, winds, core overshooting, and mixing length within a reasonable range of values, we find no single ejecta-mass–radius relation.

It remains possible that detailed spectral modeling will lend insights that might aid in uniquely determining explosion properties from plateau observations. Additionally, velocity observations before day ≈ 20 or photospheric radii derived from shock-cooling models with a secure density structure in the outer $< 0.1 M_{\odot}$ remain other promising paths forward to breaking the remaining degeneracies exhibited here.

We thank Bill Paxton for continued support and advancement of MESA’s capabilities, and Josiah Schwab and Benny Tsang for conversations and guidance. We thank the referees for helpful comments that significantly improved our presentation. We thank József Vinkó and Tamás Szalai for providing bolometric data for SN2017eaw. It is a pleasure also to thank K. Azalee Boestrom, Daichi Hiramatsu, D. Andrew Howell, and Stefano Valenti for correspondences about observations.

J.A.G. is supported by the National Science Foundation (NSF) GRFP grant No. 1650114. The MESA project is supported by the NSF under the Software Infrastructure for Sustained Innovation program grant ACI-1663688. This research was supported in part by the Gordon and Betty Moore Foundation through Grant GBMF5076 and at the KITP by the NSF under grant PHY-1748958. We acknowledge the use of computational facilities through the Center for Scientific Computing at the CNSI, MRL: an NSF MRSEC (DMR-1720256) and NSF CNS-1725797.

This research made extensive use of the SAO/NASA Astrophysics Data System (ADS).

Software: MESA, STELLA, py_mesa_reader (Wolf & Schwab 2017), SciPy (Virtanen et al. 2020), matplotlib (Hunter 2007).

ORCID iDs

Jared A. Goldberg  <https://orcid.org/0000-0003-1012-3031>

References

- Andrews, J. E., Sand, D. J., Valenti, S., et al. 2019, *ApJ*, **885**, 43
- Blinnikov, S., Lundqvist, P., Bartunov, O., Nomoto, K., & Iwamoto, K. 2000, *ApJ*, **532**, 1132
- Blinnikov, S. I., Eastman, R., Bartunov, O. S., Popolitov, V. A., & Woosley, S. E. 1998, *ApJ*, **496**, 454
- Blinnikov, S. I., Röpke, F. K., Sorokina, E. I., et al. 2006, *A&A*, **453**, 229
- Chiavassa, A., Freytag, B., Masseron, T., & Plez, B. 2011, *A&A*, **535**, A22
- Crockett, R. M., Smartt, S. J., Pastorello, A., et al. 2011, *MNRAS*, **410**, 2767
- Davies, B., & Beasor, E. R. 2018, *MNRAS*, **474**, 2116
- Dessart, L., & Hillier, D. J. 2019, *A&A*, **625**, A9
- Duffell, P. C. 2016, *ApJ*, **821**, 76
- Eldridge, J. J., Guo, N. Y., Rodrigues, N., Stanway, E. R., & Xiao, L. 2019, *PASA*, **36**, e041
- Farrell, E., Groh, J., Meynet, G., & Eldridge, J. 2020, *MNRAS: Letters*, **494**, L53
- Goldberg, J. A., Bildsten, L., & Paxton, B. 2019, *ApJ*, **879**, 3
- Goldberg, J. A., Bildsten, L., & Paxton, B. 2020, *ApJ*, **891**, 15
- Hamuy, M., & Pinto, P. A. 2002, *ApJL*, **566**, L63
- Hendry, M. A., Smartt, S. J., Crockett, R. M., et al. 2006, *MNRAS*, **369**, 1303
- Hunter, J. D. 2007, *CSE*, **9**, 90
- Kasen, D., & Woosley, S. E. 2009, *ApJ*, **703**, 2205
- Kilpatrick, C. D., & Foley, R. J. 2018, *MNRAS*, **481**, 2536
- Li, W., van Dyk, S. D., Filippenko, A. V., & Cuillandre, J.-C. 2005, *PASP*, **117**, 121
- Litvinova, I. Y., & Nadyozhin, D. K. 1983, *Ap&SS*, **89**, 89
- Martinez, L., & Bersten, M. C. 2019, *A&A*, **629**, A124
- Moriya, T. J., Förster, F., Yoon, S.-C., Gräfener, G., & Blinnikov, S. I. 2018, *MNRAS*, **476**, 2840
- Morozova, V., Piro, A. L., Fuller, J., & van Dyk, S. D. 2020, *ApJL*, **891**, L32
- Morozova, V., Piro, A. L., Renzo, M., & Ott, C. D. 2016, *ApJ*, **829**, 109
- Morozova, V., Piro, A. L., & Valenti, S. 2017, *ApJ*, **838**, 28
- Müller, T., Prieto, J. L., Pejcha, O., & Clocchiatti, A. 2017, *ApJ*, **841**, 127
- Nadyozhin, D. K. 1994, *ApJS*, **92**, 527
- Nakar, E., Poznanski, D., & Katz, B. 2016, *ApJ*, **823**, 127
- Paxton, B., Bildsten, L., Dotter, A., et al. 2011, *ApJS*, **192**, 3
- Paxton, B., Cantiello, M., Arras, P., et al. 2013, *ApJS*, **208**, 4
- Paxton, B., Marchant, P., Schwab, J., et al. 2015, *ApJS*, **220**, 15
- Paxton, B., Schwab, J., Bauer, E. B., et al. 2018, *ApJS*, **234**, 34
- Paxton, B., Smolec, R., Schwab, J., et al. 2019, *ApJS*, **243**, 10
- Pejcha, O., & Prieto, J. L. 2015, *ApJ*, **799**, 215
- Popov, D. V. 1993, *ApJ*, **414**, 712

- Renzo, M., Ott, C. D., Shore, S. N., & de Mink, S. E. 2017, [A&A](#), **603**, A118
- Ricks, W., & Dwarkadas, V. V. 2019, [ApJ](#), **880**, 59
- Rui, L., Wang, X., Mo, J., et al. 2019, [MNRAS](#), **485**, 1990
- Sahu, D. K., Anupama, G. C., Srividya, S., & Muneer, S. 2006, [MNRAS](#), **372**, 1315
- Sapir, N., & Waxman, E. 2017, [ApJ](#), **838**, 130
- Smartt, S. J. 2009, [ARA&A](#), **47**, 63
- Smartt, S. J. 2015, [PASA](#), **32**, e016
- Sukhbold, T., Ertl, T., Woosley, S. E., Brown, J. M., & Janka, H.-T. 2016, [ApJ](#), **821**, 38
- Szalai, T., Vinkó, J., Könyves-Tóth, R., et al. 2019, [ApJ](#), **876**, 19
- Takáts, K., Pignata, G., Pumo, M. L., et al. 2015, [MNRAS](#), **450**, 3137
- Tikhonov, N. A. 2014, [AstrL](#), **40**, 537
- Tsvetkov, D. Y., Shugarov, S. Y., Volkov, I. M., et al. 2018, [AstrL](#), **44**, 315
- Valenti, S., Howell, D. A., Stritzinger, M. D., et al. 2016, [MNRAS](#), **459**, 3939
- van Dyk, S. D., Zheng, W., Maund, J. R., et al. 2019, [ApJ](#), **875**, 136
- Virtanen, P., Gommers, R., Oliphant, T. E., et al. 2020, [Nat. Methods](#), **17**, 261
- Wolf, B., & Schwab, J. 2017, [wmmwolf/py_mesa_reader: Interact with MESA Output](#), Zenodo, doi: 10.5281/zenodo.826958,